Journal of Zhejiang University-SCIENCE A (Applied Physics & Engineering)
ISSN 1673-565X (Print); ISSN 1862-1775 (Online)
www.jzus.zju.edu.cn; www.springerlink.com
E-mail: jzus@zju.edu.cn

# Continuum damage modeling and progressive failure analysis of a Type III composite vessel by considering the effect of autofrettage*

Bin-bin LIAO[1], Dong-liang WANG[1], Li-yong JIA[3], Jin-yang ZHENG[†‡1,2], Chao-hua GU[1]

[1]*Institute of Process Equipment, Zhejiang University, Hangzhou 310027, China*

[2]*State Key Laboratory of Fluid Power and Mechatronic Systems, Zhejiang University, Hangzhou 310027, China*

[3]*First Aircraft Institute of Aviation Industry Corporation, Xi'an 710089, China*

[†]E-mail: jyzh@zju.edu.cn

Received Mar. 9, 2018; Revision accepted Aug. 13, 2018; Crosschecked Nov. 10, 2018; Published online Dec. 19, 2018

**Abstract:** This paper aims to study the damage mechanisms and mechanical responses of a Type III composite vessel by considering the effect of autofrettage. Firstly, damage models using Hashin failure criteria and 3D strain-based damage evolution laws for composite layers are implemented by implicit finite element codes using ABAQUS-UMAT (user material subroutine module). Secondly, the appropriate autofrettage pressure is determined by finite element analysis (FEA), in which the fiber stress ratio and the generated residual stress in the aluminium liner are investigated according to the related regulations. Finally, the effects of the autofrettage process on the internal pressure-displacement curves and damage evolution behaviors for matrix and fiber are discussed. For a composite vessel after autofrettage, the stresses in the composite layers and aluminium liner are also explored. Results show that the progressive damage evolution behaviors of the composite vessel with autofrettage and without autofrettage are basically consistent except there is some difference during the unloading process and the repressurization process in respect of matrix damage.

**Key words:** Composite vessel; Damage evolution behaviors; Hashin failure criteria; Finite element analysis (FEA)
https://doi.org/10.1631/jzus.A1800152 **CLC number:** TH49

## 1 Introduction

Composite vessels are being increasingly employed to store compressed natural gas (CNG) and hydrogen as energy sources for fuel cell vehicles, because they exhibit many advantages such as high strength- and stiffness-to-weight ratios, excellent resistance to fatigue and corrosion as well as satisfactory durability (Vasiliev et al., 2003; Zheng and Liu, 2008). The composite filament wound technology has been introduced to promote the design and manufacture of composite vessels (Liu et al., 2009; Zheng et al., 2013; Wang et al., 2015; Xiao et al., 2017). Thus, Type III composite vessels can be made as aluminium-carbon fiber/epoxy composite laminated structures by placing the composite layers with different thickness and different ply orientations as applicable to various working conditions (Zheng et al., 2009; Liu et al., 2012a; Wang et al., 2015).

Many failure criteria (Tsai and Wu, 1971; Hashin and Rotem, 1973; Hashin, 1981; Puck and Schürmann, 2002) and related damage evolution laws based on continuum damage mechanics (CDM) have been used for composites during the past decades. For example, Kim et al. (2017) predicted the nonlinear impact responses for glass fiber reinforced thermoplastic composites based on the Hashin

‡ Corresponding author

* Project supported by the National Key Research and Development Program of China (No. 2017YFC0805601)

ORCID: Bin-bin LIAO, https://orcid.org/0000-0003-2341-8082

criteria, and Liu et al. (2016) explored the dynamic progressive failure properties of composite laminates under low velocity impact using the Puck criteria. For composite vessels, many scholars have also used the CDM method to perform progressive failure analysis on the mechanical responses by finite element analysis (FEA). Onder et al. (2009) investigated the burst failure load of composite vessels by using maximum strain and stress criteria. Rafiee et al. (2015a, 2015b) explored the functional failure of glass fiber reinforced polyester (GRP) pipes under internal hydrostatic pressure. Gentilleau et al. (2015) presented a probabilistic damage behavior law for composite material used in a hydrogen storage vessel. Son and Chang (2012) evaluated the modeling techniques and explored the stress distributions in the composite layers of thick composite vessels.

However, this work has mainly studied the ultimate load-bearing ability and the burst pressure of composite vessels, and has not paid attention to the process of progressive damage evolution for fiber and matrix with increasing load. Besides, by comparison with the Type IV composite vessel, the Type III composite vessel with aluminium liner employs the autofrettage technique to enhance the static and fatigue strengths (Son et al., 2012). Hu and Chandrashekhara (2009) investigated the liner failure of composite vessels by considering the autofrettage process, and Jahromi et al. (2010) explored the stress and strain distributions induced by the autofrettage process, but they did not study the progressive failure properties and damage evolution behaviors of Type III composite vessels by considering the effect of autofrettage.

Although Son et al. (2012) determined the autofrettage pressure according to the related regulations by using FEA, they did not consider damage evolution behavior after initial failure. A more accurate modeling technique is needed because the autofrettage process involves anisotropic composite behavior and plastic deformation (Hu and Chandrashekhara, 2009; Jahromi et al., 2010). In addition, fundamental research into the progressive failure properties of the composites is essential for the optimal design of composite vessels (Kim et al., 2005; Xu et al., 2010; Liu et al., 2012b). Complex failure patterns such as matrix cracking, fiber/matrix interface debonding, and fiber breakage occur before the complete failure of composite vessels (Rafiee and Reshadi, 2014; Rafiee and Amini, 2015; Wang et al., 2015). Therefore, it is important to develop robust numerical techniques by FEA. Integrated simulation by FEA as a challenging work involves geometry, material, and boundary nonlinearities, which generally relate to the damage constitutive model, the failure criteria, and the damage evolution law (Liu et al., 2016). There has been some theoretical work using FEA on progressive analysis for composite vessels (Ju et al., 2007; Onder et al., 2009; Francescato et al., 2012; Hong et al., 2014; Wang et al., 2015), but so far it shows insufficiently accurate and mature prediction of the mechanical responses of the structures. There are two reasons for that: (1) Many predictions on the behavior of the composite pressure vessels are based on maximum strain and stress criteria (Onder et al., 2009), Tsai and Wu failure criteria (Son et al., 2012), and 2D stress-based Hashin criteria (Liu et al., 2014; Wang et al., 2015), but maximum strain and stress criteria are more efficient in the case of isotropic materials, Tsai and Wu failure criteria cannot identify the detailed failure modes, and 2D stress-based Hashin criteria fail to consider out-plane stress for a thick composite vessel. (2) Damage evolution laws were not introduced such as Ju et al. (2007), Son et al. (2012), and Hong et al. (2014).

This paper aims to study mechanical responses and damage mechanisms of a Type III composite vessel by considering the effect of autofrettage. It is important to consider damage mechanisms for fiber and matrix in depth, where the Hashin failure criteria and 3D strain-based damage evolution laws for fiber and matrix are used for composite layers. In addition, the appropriate autofrettage pressure is determined by FEA, in which the fiber stress ratio and the generated residual stress in an aluminium liner are investigated according to the related regulations about composite vessel design. The FEA is performed by implicit finite element codes using ABAQUS-UMAT (user material subroutine module). Finally, the effects of the autofrettage process on the internal pressure-displacement curves and damage evolution behaviors for the matrix and fiber are discussed. For a composite vessel after autofrettage, the stresses in composite layers and aluminium liner are also explored.

## 2 Theoretical models

### 2.1 Constitutive relationships of composites

A multi-layered composite vessel can be considered by 3D stress analysis as a cylindrical part with closed-end conditions. A local cylindrical coordinate system with radical, hoop, and axial directions ($r$, $\theta$, $z$) is defined in ABAQUS. Fig. 1 describes the principal direction (1, 2, 3) for a composite layer under the cylindrical coordinate, where $\alpha$ is the winding angle. The off-axis stress-strain relationships of the $k$th ($k$=1, 2, …, $n_s$) layer under the cylindrical coordinate system are expressed in (Xia et al., 2001; Zheng and Liu, 2008; Bakaiyan et al., 2009), where $n_s$ is the number of composite layers.

$$\begin{Bmatrix}\sigma_z\\ \sigma_\theta\\ \sigma_r\\ \tau_{\theta r}\\ \tau_{zr}\\ \tau_{z\theta}\end{Bmatrix}^{(k)}=\begin{bmatrix}\bar{C}_{11} & \bar{C}_{12} & \bar{C}_{13} & 0 & 0 & \bar{C}_{16}\\ \bar{C}_{12} & \bar{C}_{22} & \bar{C}_{23} & 0 & 0 & \bar{C}_{26}\\ \bar{C}_{13} & \bar{C}_{23} & \bar{C}_{33} & 0 & 0 & \bar{C}_{36}\\ 0 & 0 & 0 & \bar{C}_{44} & \bar{C}_{45} & 0\\ 0 & 0 & 0 & \bar{C}_{45} & \bar{C}_{55} & 0\\ \bar{C}_{16} & \bar{C}_{26} & \bar{C}_{36} & 0 & 0 & \bar{C}_{66}\end{bmatrix}^{(k)}\begin{Bmatrix}\varepsilon_z\\ \varepsilon_\theta\\ \varepsilon_r\\ \gamma_{\theta r}\\ \gamma_{zr}\\ \gamma_{z\theta}\end{Bmatrix}^{(k)}, \tag{1}$$

where $\bar{C}_{ij}$ ($i$, $j$=1, 2, …, 6) are the off-axis stiffness components. $\sigma$ and $\tau$ denote the normal and shear stresses, and $\varepsilon$ and $\gamma$ are the normal and shear strains, respectively. $\boldsymbol{C}$ is the on-axis elastic constants and the detailed expressions refer to Liu et al. (2016). The transformation of the stiffness matrix $\boldsymbol{C}$ from the on-axis coordinate system to an off-axis stiffness matrix $\bar{\boldsymbol{C}}$ can be obtained by using a stiffness transformation matrix as shown in Appendix A.

### 2.2 Damaged stress-strain relationships, failure criteria, and damage evolution laws of composites

In this research, energy-based CDM models are implemented in the finite element model to predict the damage of the composite layers. The effective stress tensor $\bar{\boldsymbol{S}}$ and the nominal stress tensor $\boldsymbol{S}$ for damaged composite layers can be written as Eq. (2) (Liu et al. 2016). The relationship between two stresses in Eq. (2) was given by Liu et al. (2016), shown in Eq. (4).

$$\bar{\boldsymbol{S}}=\boldsymbol{C}:\boldsymbol{E},\quad \boldsymbol{S}=\boldsymbol{C}_{\mathrm{d}}:\boldsymbol{E}, \tag{2}$$

$$\boldsymbol{C}=\frac{1}{\Omega}\times\begin{bmatrix}E_1(1-\nu_{23}\nu_{32}) & E_2(\nu_{12}-\nu_{13}\nu_{32}) & E_3(\nu_{13}-\nu_{12}\nu_{23}) & & & \\ E_1(\nu_{21}-\nu_{31}\nu_{23}) & E_2(1-\nu_{13}\nu_{31}) & E_3(\nu_{23}-\nu_{21}\nu_{13}) & & & \\ E_1(\nu_{31}-\nu_{21}\nu_{32}) & E_2(\nu_{32}-\nu_{12}\nu_{31}) & E_3(1-\nu_{12}\nu_{21}) & & & \\ & & & \Omega G_{12} & & \\ & & & & \Omega G_{23} & \\ & & & & & \Omega G_{13}\end{bmatrix},$$

$$\Omega=1-\nu_{12}\nu_{21}-\nu_{23}\nu_{32}-\nu_{31}\nu_{13}-2\nu_{12}\nu_{23}\nu_{31}, \tag{3}$$

$$\begin{Bmatrix}\bar{S}_{11}\\ \bar{S}_{22}\\ \bar{S}_{33}\\ \bar{S}_{12}\\ \bar{S}_{13}\\ \bar{S}_{23}\end{Bmatrix}=\begin{bmatrix}\frac{1}{1-d_{11}} & 0 & 0 & 0 & 0 & 0\\ 0 & \frac{1}{1-d_{22}} & 0 & 0 & 0 & 0\\ 0 & 0 & 1 & 0 & 0 & 0\\ 0 & 0 & 0 & \frac{1}{1-d_{12}} & 0 & 0\\ 0 & 0 & 0 & 0 & \frac{1}{1-d_{13}} & 0\\ 0 & 0 & 0 & 0 & 0 & \frac{1}{1-d_{23}}\end{bmatrix}\begin{Bmatrix}S_{11}\\ S_{22}\\ S_{33}\\ S_{12}\\ S_{13}\\ S_{23}\end{Bmatrix}, \tag{4}$$

where $\boldsymbol{C}$ is the undamaged elastic tensor and $\boldsymbol{C}_{\mathrm{d}}$ is the damaged elastic tensor. $E_1$, $E_2$, and $E_3$ are Young's moduli and $G_{12}$, $G_{23}$, and $G_{13}$ are shear moduli. $E_{ij}$ ($i$, $j$=1, 2, 3) is the component of the strain tensor $\boldsymbol{E}$. $\nu_{ij}$ ($i$, $j$=1, 2, 3) is Poisson's ratio. The expressions for the damage variables $d_{ij}$ ($ij$ indicates 11, 22, 33, 12, 23, 31) see Liu et al. (2016).

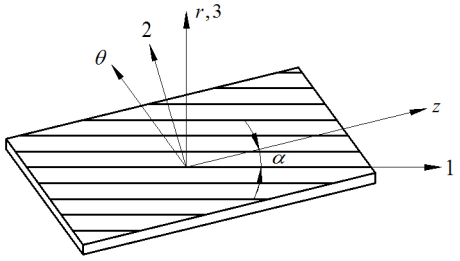


**Fig. 1 On-axis coordinate (1, 2, 3) and the off-axis coordinate ($r$, $\theta$, $z$) for a composite layer**

Fiber and matrix may be defined by the stress- or strain-based failure criteria. Hashin (1981) proposed fiber and matrix failure criteria based on stress. Huang and Lee (2003) showed strain may be a better choice for defining the failure of composites because strain is more continuous by comparison with stress during damage evolution (Liu et al., 2016). Li et al. (2014) further proposed strain-based Hashin criteria for four failure modes of composites, and those are used in this study.

1. Fiber tension and compression

$$\begin{cases} \left(F_{11}^{\mathrm{T}}\right)^2=\left(\dfrac{E_{11}}{E_{0,1}^{\mathrm{T}}}\right)^2+\left(\dfrac{E_{12}}{E_{0,12}}\right)^2+\left(\dfrac{E_{13}}{E_{0,13}}\right)^2\geqslant 1, \\ \left(F_{11}^{\mathrm{C}}\right)^2=\left(\dfrac{E_{11}}{E_{0,1}^{\mathrm{C}}}\right)^2\geqslant 1, \end{cases} \tag{5}$$

where $F_{11}$ denotes the fiber failure index. The superscripts "T" and "C" denote tension and compression, respectively. $E_{0,1}^{\mathrm{T}}$ and $E_{0,1}^{\mathrm{C}}$ are the initial failure strains for fiber tension and compression. $E_{0,12}$ and $E_{0,13}$ are the initial in-plane and out-plane shear failure strains, respectively.

$$E_{0,1}^{\mathrm{T}}=\frac{X^{\mathrm{T}}}{E_1},\ E_{0,1}^{\mathrm{C}}=\frac{X^{\mathrm{C}}}{E_1},\ E_{0,12}=\frac{\hat{S}_{12}}{G_{12}},\ E_{0,13}=\frac{\hat{S}_{13}}{G_{13}}, \tag{6}$$

where $X^{\mathrm{T}}$ and $X^{\mathrm{C}}$ are the fiber tensile and compressive strengths, respectively. $\hat{S}_{12}$ is the in-plane shear strength and $\hat{S}_{13}$ is the out-of-plane shear strength.

For fiber tension and compression, the damage evolution laws are assumed by

$$d_{11}^{\mathrm{T(C)}}=1-\frac{1}{F_{11}^{\mathrm{T(C)}}}\exp\left[\left(1-F_{11}^{\mathrm{T(C)}}\right)\frac{\left(X^{\mathrm{T(C)}}\right)^2 l}{E_1\Gamma_{11}^{\mathrm{T(C)}}}\right]. \tag{7}$$

A characteristic length $l$ is introduced to solve the critical failure strain through regularizing the fiber fracture energy $\Gamma_{11}^{\mathrm{T(C)}}$ in order to eliminate the mesh sensitivity problem (Tan et al., 2015; Liu et al., 2016). Besides, fiber compression is induced by a microbuckling mechanism such as kink band and it decreases the load-bearing abilities of composites. But fiber compression does not result in global collapse (Liu et al., 2016). The residual strength, i.e. fiber crushing strength $X^{\mathrm{res}}$ is equal to the matrix compressive strength (Liu et al., 2016). Therefore, the damage mechanisms for fiber tension and compression are basically the same (Liu et al., 2016).

2. Matrix tension

$$\begin{cases} \left(F_{22}^{\mathrm{T}}\right)^2=\dfrac{\left(E_{22}+E_{33}\right)^2}{\left(E_{0,2}^{\mathrm{T}}\right)^2}-\dfrac{E_{22}E_{33}}{\left(E_{0,23}\right)^2} \\ \qquad\qquad +\left(\dfrac{E_{12}}{E_{0,12}}\right)^2+\left(\dfrac{E_{13}}{E_{0,13}}\right)^2+\left(\dfrac{E_{23}}{E_{0,23}}\right)^2\geqslant 1, \\ E_{0,23}=\dfrac{\hat{S}_{23}}{G_{23}},\ E_{0,2}^{\mathrm{T}}=\dfrac{Y^{\mathrm{T}}}{E_2}, \end{cases} \tag{8}$$

where $F_{22}$ is the matrix failure index. $E_{0,2}^{\mathrm{T}}$ is the initial tension failure strain of the matrix, $E_{0,23}$ is the initial out-of-plane shear strain, $\hat{S}_{23}$ is the out-of-plane shear strength, and $Y^{\mathrm{T}}$ is the matrix tensile strength.

For matrix tension, the damage evolution law is written as

$$d_{22}^{\mathrm{T}}=1-\frac{1}{F_{22}^{\mathrm{T}}}\exp\left[\left(1-F_{22}^{\mathrm{T}}\right)\frac{\left(Y^{\mathrm{T}}\right)^2 l}{E_2\Gamma_{22}^{\mathrm{T}}}\right], \tag{9}$$

where $\Gamma_{22}^{\mathrm{T}}$ is the tension fracture energy of the matrix.

3. Matrix compression

$$\left(F_{22}^{\mathrm{C}}\right)^2=\frac{\left(E_{22}+E_{33}\right)^2}{\left(E_{0,2}^{\mathrm{C}}\right)^2}+\frac{E_{22}+E_{33}}{E_{0,2}^{\mathrm{C}}}\left(\frac{E_{0,2}^{\mathrm{C}}}{2E_{0,12}}-1\right)-\frac{E_{22}E_{33}}{\left(E_{0,23}\right)^2} +\left(\frac{E_{12}}{E_{0,12}}\right)^2+\left(\frac{E_{13}}{E_{0,13}}\right)^2+\left(\frac{E_{23}}{E_{0,23}}\right)^2\geqslant 1, \tag{10}$$

where $E_{0,2}^{\mathrm{C}}=Y^{\mathrm{C}}/E_2$ is the initial compression failure strain of the matrix, and $Y^{\mathrm{C}}$ is the matrix compressive strength.

For matrix compression, the damage evolution law is expressed as

$$d_{22}^{\mathrm{C}}=1-\frac{1}{F_{22}^{\mathrm{C}}}\exp\left[\left(1-F_{22}^{\mathrm{C}}\right)\frac{\left(Y^{\mathrm{C}}\right)^2 l}{E_2\Gamma_{22}^{\mathrm{C}}}\right], \tag{11}$$

where $\Gamma_{22}^{\mathrm{C}}$ is the compression fracture energy of the matrix.

Material models which exhibit stiffness degradation often generate some convergence difficulties in ABAQUS/Standard. This can be solved by using the viscous regularization method in order to make the tangent stiffness matrix to be positive definite. In the viscous regularization, a viscous damage variable is defined as (Lapczyk and Hurtado, 2007)

$$\dot{d}^{\mathrm{v}}=\frac{1}{\eta}\left(d-d^{\mathrm{v}}\right), \tag{12}$$

where $\eta$ denotes a viscous constant related to the relaxation time, and $d^{\mathrm{v}}$ is a regularized damage variable.

Standard DOT-CFFC (DOT, 2007) is considered to determinate the appropriate autofrettage pressure of a Type III composite vessel among many regulations dealing with the design and manufacture of composite vessels. Four important conditions are shown as follows:

**Condition 1** Minimum burst pressure is 3.4 times the service pressure and failure should not occur below the minimum burst pressure.

**Condition 2** Test pressure which is 5/3 times the service pressure should not exceed the autofrettage pressure.

**Condition 3** The compressive stress of the liner must be at least 60% but no more than 95% of the minimum yield strength of the liner at zero pressure.

**Condition 4** The ratio of the maximum fiber stress at the minimum burst pressure to that at the service pressure (fiber stress ratio) should be larger than 10/3.

## 3 Validation of progressive analysis approach

In order to validate the progressive failure method based on the Hashin failure criteria and 3D strain-based damage evolution laws in this study, numerical codes are developed using ABAQUS-UMAT to implement the implicit FEA algorithm. It is also compared with the experimental result (Liu et al., 2012c). T700 fiber/epoxy composite specimens with a 10 mm central hole are used in the test. The lay pattern and geometry size are $[0°/45°/90°/-45°]_{2s}$ and 250 mm×25 mm×1.8 mm, respectively. The thickness of each ply is 0.1125 mm. Material parameters for T700 fiber/epoxy composite layers are listed in Table 1.

**Table 1 Material parameters for T700 fiber/epoxy composite layers (Tan et al., 2015; Wang et al., 2015)**

| Parameter | Description |
|---|---|
| Young's moduli | $E_1$=141 GPa, $E_2$=$E_3$=11.4 GPa |
| Shear moduli | $G_{23}$=3.8 GPa, $G_{12}$=$G_{13}$=7.1 GPa |
| Poisson's ratio | $v_{12}$=$v_{13}$=0.28, $v_{23}$=0.4 |
| Strength parameters | $X^{\mathrm{T}}$=2080 MPa, $X^{\mathrm{C}}$=1250 MPa, $Y^{\mathrm{T}}$=60 MPa, $Y^{\mathrm{C}}$=290 MPa, $\hat{S}_{12}=\hat{S}_{13}=\hat{S}_{23}=110$ MPa |
| Fracture toughness | $\Gamma_{11}^{\mathrm{T}}=133$ N/mm, $\Gamma_{11}^{\mathrm{C}}=40$ N/mm, $\Gamma_{22}^{\mathrm{T}}=0.6$ N/mm, $\Gamma_{22}^{\mathrm{C}}=1.6$ N/mm |

The laminates are continuously loaded under displacement control. The stress-strain curves obtained numerically are shown in Fig. 2. The numerical result is in good agreement with the experimental result (Liu et al., 2012c). Fiber damage and matrix damage are defined by two damage variables SDV1 and SDV2 in ABAQUS-UMAT, respectively. Fig. 3 shows the fiber damage and matrix damage of 0° and 90° plies. Fiber damage of the 0° ply initiates at the blunt notch and then propagates perpendicular to the loading direction. Most of the fiber damage appears at the 0° ply, but matrix damage in the 90° ply is more severe than that in the 0° ply, which is consistent with the conclusions obtained by Lapczyk and Hurtado (2007).

## 4 Results and discussion

### 4.1 Finite element model for the composite vessel

The composite vessel as shown in Fig. 4 is composed of a 6061-T6 aluminium liner and T700 fiber/epoxy composite layers. The helical and hoop windings occur at the cylinder but only the helical

winding appears at the head of the vessel (Liu et al., 2009). The helical winding at the head obeys the geodesic path algorithm, which marks the shortest distance between any two points on the surface of the head (Liu et al., 2012a). The helical winding angle $\alpha$ varies from 90° at the polar axis to $\alpha_0$ at the cylinder. The thickness $H$ of the composite layer at any radius $R$ of the head is calculated by Xu et al. (2010) and Liu et al. (2012b).

$$\begin{cases}\alpha = \arcsin(\lambda / R), \\ H = h\sqrt{(R_0^2 - \lambda^2)/(R^2 - \lambda^2)},\end{cases} \tag{13}$$

where $\lambda$ represents the polar axis radius, $h$ is the helical winding thickness of the cylinder, and $R_0$ denotes the inner radius of the cylinder.

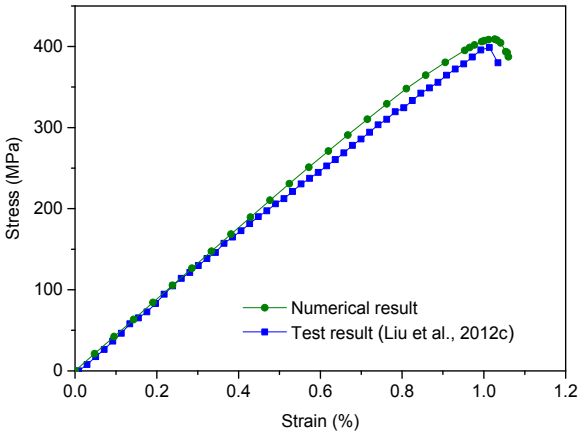


**Fig. 2 Stress-strain curves of the $[0°/45°/90°/-45°]_{2s}$ specimen**

Fig. 4 shows the finite element mesh model of the vessel. The geometry parameters of the composite vessel are listed in Table 2. Only half of the vessel is modeled by consideration of the symmetry of the vessel structure, and appropriate load conditions and symmetric boundary are specified for the vessel. In this finite element model, the aluminium liner and the composite layers are modeled using the reduced integration element C3D8R, enhanced hourglass control, and distortion control. With the element size 2 mm×2 mm, 8832 bulk elements are included in the aluminium liner, and 109 760 bulk elements with the element size 0.9 mm×0.9 mm are included in the composite layers. The aluminium liner and the composite layers are tied together. In order to balance the numerical error and convergence, the viscous stabilization method with viscous constant 0.001 is adopted to obtain the ultimate load capacity of the composite vessel effectively. The aluminium liner is considered to be isotropic and

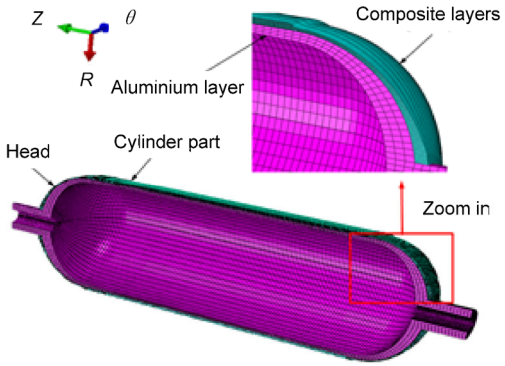


**Fig. 4 Finite element model of the composite vessel**

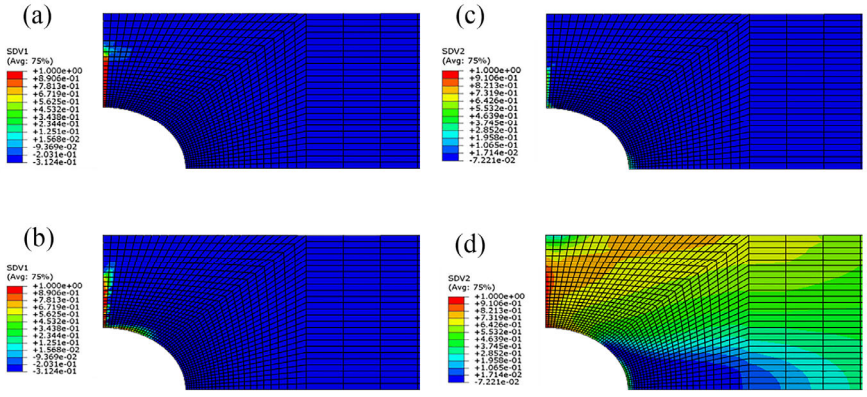


**Fig. 3 Fiber damage and matrix damage of 0° and 90° plies**

(a) Fiber damage in 0° ply; (b) Matrix damage in 0° ply; (c) Fiber damage in 90° ply; (d) Matrix damage in 90° ply

elastic-plastic. The stress-strain curves for aluminium obtained from experiments are shown in Fig. 5. The elastic modulus and Poisson's ratio of the aluminium are 70 GPa and 0.33, respectively. The yield strength is about 298 MPa. Material parameters for transversely isotropic composite layers are the same as the values in Table 1.

**Table 2 Geometry parameters of the composite vessel**

| Inner diameter (mm) | Layer No. | Layer angle (°) | Layer thickness (mm) |
|---|---|---|---|
| 95 | Al | – | 2.50 |
| 95 | L1 | 90 | 0.32 |
| 95 | L2 | 14 | 0.18 |
| 95 | L3 | −14 | 0.18 |
| 95 | L4 | 90 | 0.32 |
| 95 | L5 | 14 | 0.18 |
| 95 | L6 | −14 | 0.18 |
| 95 | L7 | 90 | 0.32 |
| 95 | L8 | 14 | 0.18 |
| 95 | L9 | −14 | 0.18 |
| 95 | L10 | 90 | 0.32 |

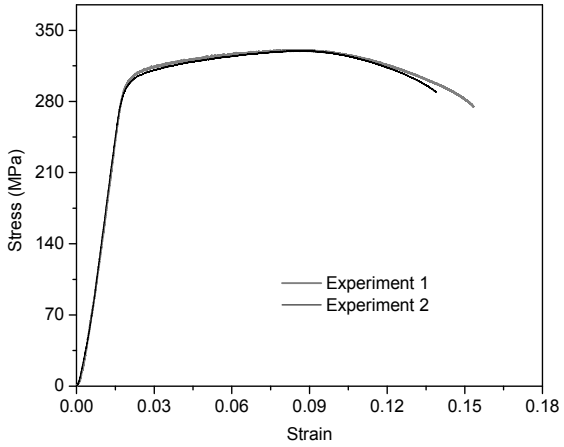


**Fig. 5 Stress-strain curves for aluminium**

## 4.2 Determination of the appropriate autofrettage pressure

A multifunctional pressure test system with a high pressure pump is used for the burst experiment and the ascending velocity of the pressure is 0.2 MPa/s. Fig. 6 shows the monitored pressure against the filling time during the test. The pressure increases approximately linearly until it drops to zero suddenly, which indicates the burst failure of the vessel. The maximum pressure, 74 MPa, during the test is the burst pressure. The predicted failure strength based on the Hashin criteria is 71 MPa and the details are shown in Section 4.3. The numerical result is in good agreement with the experimental result of 74 MPa in Fig. 6. It is shown that the progressive failure method in this study can predict the mechanical responses and the ultimate load-bearing ability accurately. Then, we determine the appropriate autofrettage pressure based on this method by FEA.

The service pressure should be 20 MPa based on Conditions 1 and 2 (DOT, 2007), and the autofrettage pressure should be larger than 33 MPa. To check Conditions 3 and 4 (DOT, 2007), the load history in Fig. 7 should be imposed on the vessel and it is divided into four steps. Steps 1 and 2 are the autofrettage processes with the vessel pressurized from zero pressure to the autofrettage pressure in Step 1 and then unloaded to zero pressure in Step 2. Steps 3 and 4 are the repressurization processes with the pressure rising from zero pressure to the service pressure, 20 MPa, in Step 3, and from 20 MPa to the minimum burst pressure in Step 4. At the zero pressure condition, the service pressure condition, and the minimum burst pressure condition, fiber stress and liner stress are calculated. After examining all the conditions as follows, the appropriate autofrettage pressure is determined.

Fig. 8a shows the maximum fiber stress and maximum liner stress under service pressure and minimum burst pressure conditions against the autofrettage pressure. The maximum liner stresses at service pressure decrease as the autofrettage pressure

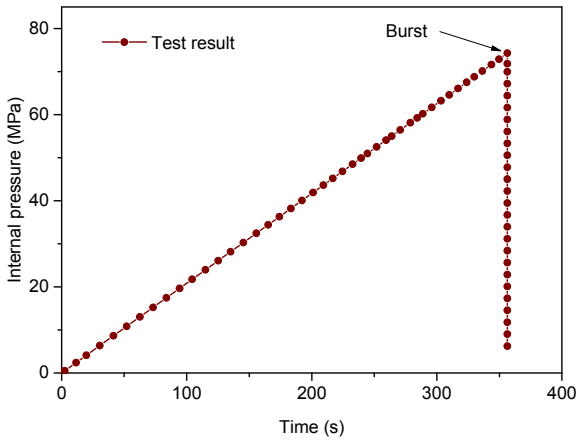


**Fig. 6 Monitored pressure in the composite vessel during the burst experiment**

increases to 44 MPa and then remain basically unchanged. The maximum stresses generated in the liner all attain nearly their ultimate strength under the minimum burst pressure. The maximum fiber stresses in the composite layers increase linearly against the autofrettage pressure at the service pressure and they show basically the same at the minimum burst pressure, which shows that autofrettage basically does not change the ultimate load-bearing ability of the vessel.

Fig. 8b shows the maximum liner stress at zero pressure of Step 2 and the fiber stress ratio against the autofrettage pressure. The maximum liner stresses at zero pressure increase linearly as the autofrettage pressure increases. The reason is that a greater plastic strain is generated in the liner at a higher autofrettage pressure, which leads to larger residual liner stress after the autofrettage process. Based on Condition 3 (DOT, 2007), the maximum liner stress at zero pressure should be in the range of 178.8 MPa to 283.1 MPa, which causes the autofrettage pressure to be larger than 41.6 MPa at least. To check Condition 4 (DOT, 2007), the fiber stress ratio calculated from Fig. 8a should be greater than 10/3. Thus, the autofrettage pressure should be less than 45.5 MPa by consideration of the theoretically safety. After examining all the conditions (DOT, 2007), the appropriate autofrettage pressure is determined as 45 MPa in order to minimize the liner stress and make full use of carbon fibers at service pressure.

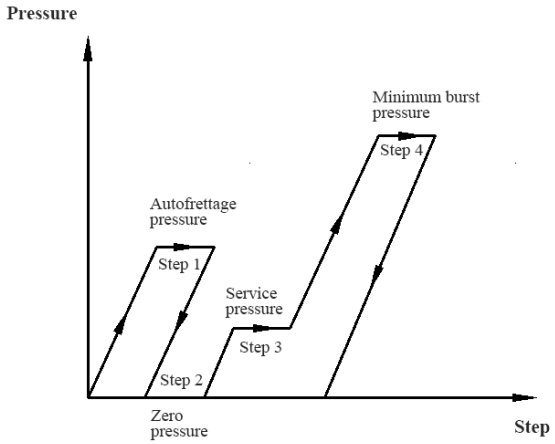


**Fig. 7 Loading history for the composite vessel with autofrettage**

### 4.3 Results for progressive failure analysis with autofrettage

Fig. 9 shows the internal pressure versus displacement curves with autofrettage and without autofrettage. The responses of the vessel with autofrettage in the axial and radial directions are almost the same as the vessel without autofrettage except the unloading process and the repressurization process from zero pressure to 45 MPa. The curves give four distinct regions before the sudden drop in Fig. 6. The first linear curves before 25 MPa denote the initial elastic behavior of the materials, the following nonlinear curves denote the plastic deformation of the aluminium liner, the third approximately linear curves from about 40 MPa indicate that matrix

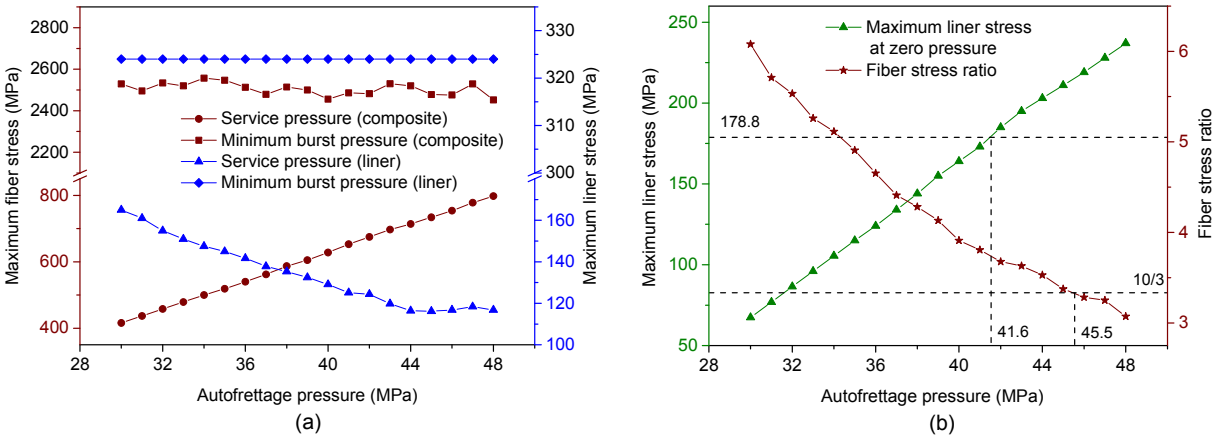


**Fig. 8 Stress analysis for determining the appropriate autofrettage pressure**

(a) Maximum fiber stress and maximum liner stress at service pressure and minimum burst pressure conditions; (b) Maximum liner stress at zero pressure and the fiber stress ratio

damage appears, and finally nearly flat curves suggest that fiber damage occurs at about 69 MPa and the advent of burst. At about 71 MPa, the displacements of radial and axial directions increase and the burst pressure basically remains unchanged, indicating that the vessel bursts. From Fig. 9, the damage evolution with autofrettage can be divided into two levels. The first level indicates only matrix damage as shown in Fig. 10, and in the second level the fiber damage appears as shown in Fig. 11. Fiber damage and matrix damage are also defined by two damage variables SDV1 and SDV2 in ABAQUS-UMAT, respectively.

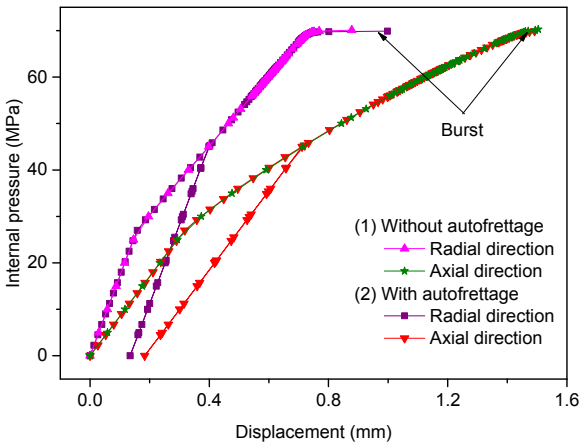


**Fig. 9 Predicted load-displacement curves of the vessel with and without autofrettage**

From Fig. 10a, matrix damage appears initially at the helical layers with pressure rising at about 40 MPa in Step 1. There are two reasons as follows: (1) The hoop stress is larger than the axial stress and radial stress under the internal pressure, similar to the conclusion obtained by Xia et al. (2001) and Bakaiyan et al. (2009). (2) Larger hoop stress generates larger tensile stress in the matrix direction of the helical layers, which is almost consistent with the hoop stress direction. By comparison, matrix damage appears initially at the inner helical composite layers and evolves from the center to the both ends of cylinder part. Fig. 10b shows matrix damage at the autofrettage pressure (45 MPa) of Step 1. The matrix damage propagates but still only appears at the helical layers. Besides, matrix damage remains unchanged during the unloading process in Step 2 and the repressurization process with the pressure rising from zero pressure to 45 MPa in Steps 3 and 4, which is the same as the matrix damage at the autofrettage pressure of the Step 1. It can be seen that matrix damage exists after autofrettage but does not exist without autofrettage at the service pressure (20 MPa). From Fig. 10c, hoop layers start to appear in matrix damage at about 60 MPa in Step 4 and the maximum

nctionally graded metal–
omposite Structures, 92(8): 1813-1822.
/10.1016/j.compstruct.2010.01.019

the helical layers, the matrix damage of hoop layers appears at higher pressure due to smaller axial stress (Xia et al., 2001; Bakaiyan et al., 2009) at the matrix direction of the hoop layers. From Figs. 11a and 11b, fiber damage appears initially at the hoop layers as the pressure reaches about 69 MPa in Step 4. The reason is that the larger hoop stress (Xia et al., 2001; Bakaiyan et al., 2009) generates larger fiber stress at hoop layers which use the hoop winding. The fiber damage evolves from the middle part to both ends of the hoop layers and mainly appears in the inner hoop layers. The matrix damage of the cylinder part basically reaches 1 at helical layers and continues to evolve at hoop layers. From Figs. 11c and 11d, with severe fiber damage appearing at the hoop layers, the helical layers begin to show fiber damage at about 70.5 MPa due to smaller axial stress. For matrix damage, both ends of the hoop layers are more severe than the middle part. Figs. 11e and 11f show the fiber damage and matrix damage at the burst pressure. In general, most of the fiber damage appears at the hoop layers, but the matrix damage at helical layers is more severe than that in the hoop layers.

Fig. 12 (p.46) shows the maximum liner stress and maximum fiber stress without autofrettage and with autofrettage, against the different internal pressures. Maximum liner stress and maximum fiber stress are basically the same after 45 MPa. It can be seen that the autofrettage process only affects the stress distribution when the pressure is lower than the autofrettage pressure. By comparison, the fiber stress increases remarkably, which means that the fiber utilization is greatly enhanced. However, the aluminium liner stress reduces significantly except in the pressure range from 0 to 10 MPa. A possible reason is that the tensile stress under internal pressure at the beginning is not enough to balance the residual stress generated at the autofrettage process.

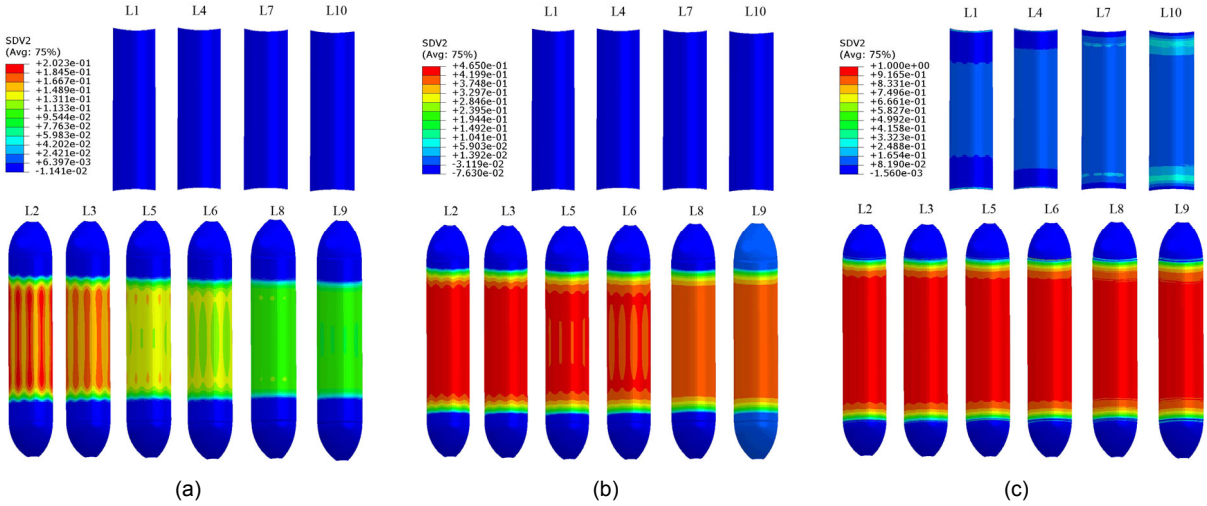


**Fig. 10 Matrix damage at 40 MPa in Step 1 (a), autofrettage pressure in Step1 (b), and 60 MPa in Step 4 (c)**

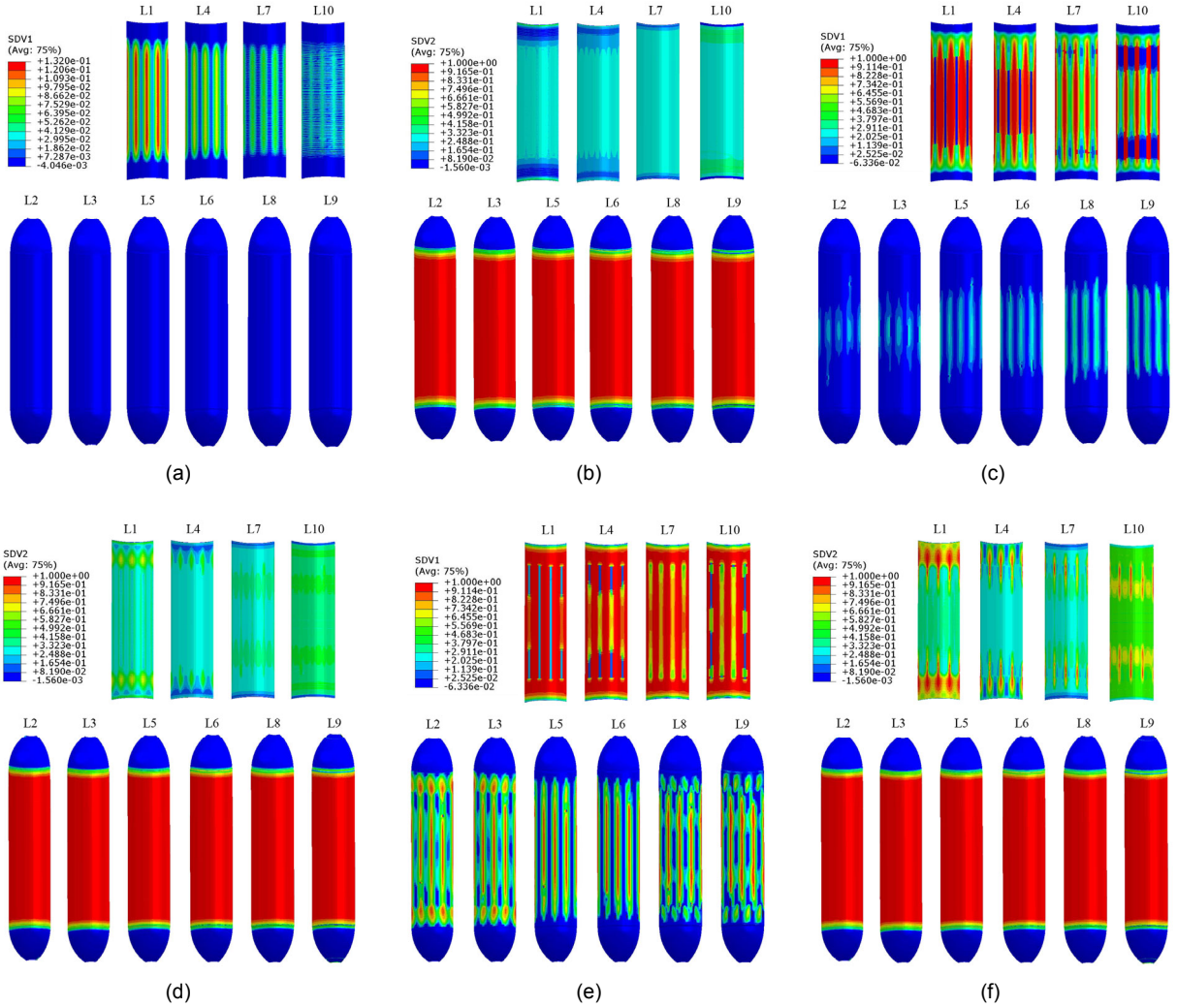


**Fig. 11 Fiber damage and matrix damage in Step 4: (a) fiber damage at 69 MPa; (b) matrix damage at 69 MPa; (c) fiber damage at 70.5 MPa; (d) matrix damage at 70.5 MPa; (e) fiber damage at 71 MPa; (f) matrix damage at 71 MPa**

Fig. 13 shows the hoop and axial aluminium liner stresses at zero and service pressures along the axial direction of the vessel without autofrettage and with autofrettage. The maximum hoop and axial liner stresses without autofrettage appear at the middle part of the cylinder which is considered to be a dangerous area for failure. By comparison, the middle of the cylinder is in compressive state at zero pressure after autofrettage, which leads to hoop and axial stresses at the middle of the cylinder at service pressure decrease by 86% and 75%, and the maximum hoop and axial liner stresses appear at both ends of cylinder near the head. Therefore, autofrettage can significantly enhance the mechanical performance of composite vessels.

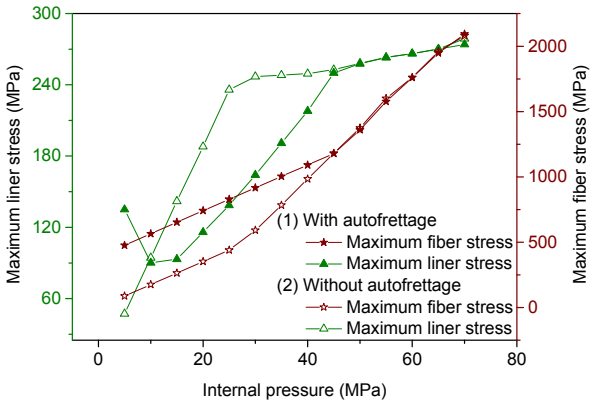


**Fig. 12 Maximum liner stress and maximum fiber stress without autofrettage and with autofrettage at different internal pressures**

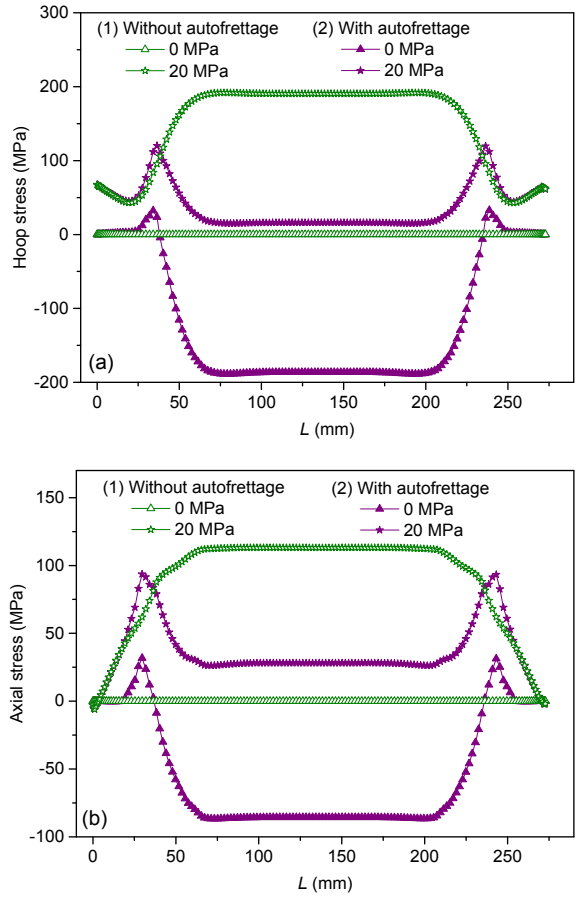


**Fig. 13 Aluminium liner stresses at zero and service pressures without autofrettage and with autofrettage: (a) hoop stress; (b) axial stress**

## 5 Conclusions

This paper studies the progressive failure mechanisms of a Type III composite vessel by considering the effect of autofrettage. Damage models with the Hashin criteria and strain-based damage evolution laws for composite layers are implemented by the implicit finite element subroutine ABAQUS-UMAT. From numerical analysis on the composite vessel with autofrettage and without autofrettage, three main conclusions are obtained:

1. Matrix damage appears initially at the helical layers but fiber damage appears initially at the hoop layers. Besides, most of the matrix damage appears at the helical layers while fiber damage at the hoop layers is more severe than at the helical layers. Both matrix damage of helical layers and fiber damage of hoop layers evolve from the middle part to the ends of the cylinder.

2. By comparison, the damage evolution behaviors of the composite vessel with autofrettage are almost consistent with the vessel without autofrettage except the unloading process and the repressurization process with the pressure rising from zero pressure to the pressure equal to the autofrettage pressure. At this stage, matrix damage remains unchanged and the same as that at the autofrettage pressure. It is obvious that matrix damage exists after autofrettage but does not exist without autofrettage at the service pressure.

3. Autofrettage process only affects the stress distribution when the internal pressure is lower than the autofrettage pressure. By comparison, although the matrix damage remains unchanged during this

stage, the aluminium liner stress reduces except the low pressure at the beginning and the fiber stress increases remarkably. In addition, the maximum hoop and axial liner stresses with autofrettage reduce significantly and appear at both ends of cylinder at service pressure.

Therefore, the appropriate autofrettage pressure for the composite vessel plays an important role in making full use of the advantages of these two materials, and an integrated design concept should commit to improving comprehensive performance of structures. Further work will focus on the multi-scale analysis of composite vessels under complex loads using FEA. However, large-scale parallel numerical computation is needed in order to promote the application of the developed numerical technique. Implicit FEA for composite vessels with large element numbers is very time-consuming. Our long-term work will continue to address some challenging issues on the damage, strength, and fracture behaviors of lightweight composite vessels under complicated environments and loads.

## References


Bakaiyan H, Hosseini H, Ameri E, 2009. Analysis of multi-layered filament-wound composite pipes under combined internal pressure and thermomechanical loading with thermal variations. *Composite Structures*, 88(4): 532-541. https://doi.org/10.1016/j.compstruct.2008.05.017

DOT (Department of Transportation), 2007. Basic Requirements for Fully Wrapped Carbon-fiber Reinforced Aluminum Lined Cylinders, DOT-CFFC. DOT, USA.

Francescato P, Gillet A, Leh D, et al., 2012. Comparison of optimal design methods for type 3 high-pressure storage tanks. *Composite Structures*, 94(6):2087-2096. https://doi.org/10.1016/j.compstruct.2012.01.018

Gentilleau B, Villalonga S, Nony F, et al., 2015. A probabilistic damage behavior law for composite material dedicated to composite pressure vessel. *International Journal of Hydrogen Energy*, 40(38):13160-13164. https://doi.org/10.1016/j.ijhydene.2015.04.043

Hashin Z, 1981. Fatigue failure criteria for unidirectional fiber composites. *Journal of Applied Mechanics*, 48(4):846-852. https://doi.org/10.1115/1.3157744

Hashin Z, Rotem A, 1973. A fatigue failure criterion for fiber reinforced materials. *Journal of Composite Materials*, 7(4):448-464. https://doi.org/10.1177/002199837300700404

Hong JH, Han MG, Chang SH, 2014. Safety evaluation of 70 MPa-capacity type III hydrogen pressure vessel considering material degradation of composites due to temperature rise. *Composite Structures*, 113:127-133. https://doi.org/10.1016/j.compstruct.2014.03.008

Hu J, Chandrashekhara K, 2009. Fracture analysis of hydrogen storage composite cylinders with liner crack accounting for autofrettage effect. *International Journal of Hydrogen Energy*, 34(8):3425-3435. https://doi.org/10.1016/j.ijhydene.2009.01.094

Huang CH, Lee YJ, 2003. Experiments and simulation of the static contact crush of composite laminated plates. *Composite Structures*, 61(3):265-270. https://doi.org/10.1016/S0263-8223(02)00047-8

Jahromi BH, Ajdari A, Nayeb-Hashemi H, et al., 2010. Autofrettage of layered and functionally graded metal–ceramic composite vessels. *Composite Structures*, 92(8): 1813-1822. https://doi.org/10.1016/j.compstruct.2010.01.019

Ju J, Pickle BD, Morgan RJ, et al., 2007. An initial and progressive failure analysis for cryogenic composite fuel tank design. *Journal of Composite Materials*, 41(21): 2545-2568. https://doi.org/10.1177/0021998307076492

Kim CU, Kang JH, Hong CS, et al., 2005. Optimal design of filament wound structures under internal pressure based on the semi-geodesic path algorithm. *Composite Structures*, 67(4):443-452. https://doi.org/10.1016/j.compstruct.2004.02.003

Kim DH, Jung KH, Lee IG, et al., 2017. Three-dimensional progressive failure modeling of glass fiber reinforced thermoplastic composites for impact simulation. *Composite Structures*, 176:757-767. https://doi.org/10.1016/j.compstruct.2017.06.031

Lapczyk I, Hurtado JA, 2007. Progressive damage modeling in fiber-reinforced materials. *Composites Part A: Applied Science and Manufacturing*, 38(11):2333-2341. https://doi.org/10.1016/j.compositesa.2007.01.017

Li DH, Liu Y, Zhang X, 2014. Low-velocity impact responses of the stiffened composite laminated plates based on the progressive failure model and the layerwise/solid-elements method. *Composite Structures*, 110:249-275. https://doi.org/10.1016/j.compstruct.2013.12.011

Liu PF, Xu P, Zheng JY, 2009. Artificial immune system for optimal design of composite hydrogen storage vessel. *Computational Materials Science*, 47(1):261-267. https://doi.org/10.1016/j.commatsci.2009.07.015

Liu PF, Chu JK, Hou SJ, et al., 2012a. Micromechanical damage modeling and multiscale progressive failure analysis of composite pressure vessel. *Computational Materials Science*, 60:137-148. https://doi.org/10.1016/j.commatsci.2012.03.015

Liu PF, Chu JK, Hou SJ, et al., 2012b. Numerical simulation and optimal design for composite high-pressure hydrogen storage vessel: a review. *Renewable and Sustainable Energy Reviews*, 16(4):1817-1827. https://doi.org/10.1016/j.rser.2012.01.006

Liu PF, Chu JK, Liu YL, et al., 2012c. A study on the failure

mechanisms of carbon fiber/epoxy composite laminates using acoustic emission. *Materials & Design*, 37:228-235. https://doi.org/10.1016/j.matdes.2011.12.015

Liu PF, Xing LJ, Zheng JY, 2014. Failure analysis of carbon fiber/epoxy composite cylindrical laminates using explicit finite element method. *Composites Part B: Engineering*, 56:54-61. https://doi.org/10.1016/j.compositesb.2013.08.017

Liu PF, Liao BB, Jia LY, et al., 2016. Finite element analysis of dynamic progressive failure of carbon fiber composite laminates under low velocity impact. *Composite Structures*, 149:408-422. https://doi.org/10.1016/j.compstruct.2016.04.012

Onder A, Sayman O, Dogan T, et al., 2009. Burst failure load of composite pressure vessels. *Composite Structures*, 89(1):159-166. https://doi.org/10.1016/j.compstruct.2008.06.021

Puck A, Schürmann H, 2002. Failure analysis of FRP laminates by means of physically based phenomenological models. *Composites Science and Technology*, 62(12-13):1633-1662. https://doi.org/10.1016/S0266-3538(01)00208-1

Rafiee R, Reshadi F, 2014. Simulation of functional failure in GRP mortar pipes. *Composite Structures*, 113:155-163. https://doi.org/10.1016/j.compstruct.2014.03.024

Rafiee R, Amini A, 2015. Modeling and experimental evaluation of functional failure pressures in glass fiber reinforced polyester pipes. *Computational Materials Science*, 96:579-588. https://doi.org/10.1016/j.commatsci.2014.03.036

Rafiee R, Fakoor M, Hesamsadat H, 2015a. The influence of production inconsistencies on the functional failure of GRP pipes. *Steel and Composite Structures*, 19(6):1369-1379. https://doi.org/10.12989/scs.2015.19.6.1369

Rafiee R, Reshadi F, Eidi S, 2015b. Stochastic analysis of functional failure pressures in glass fiber reinforced polyester pipes. *Materials & Design*, 67:422-427. https://doi.org/10.1016/j.matdes.2014.12.003

Son DS, Chang SH, 2012. Evaluation of modeling techniques for a type III hydrogen pressure vessel (70 MPa) made of an aluminum liner and a thick carbon/epoxy composite for fuel cell vehicles. *International Journal of Hydrogen Energy*, 37(3):2353-2369. https://doi.org/10.1016/j.ijhydene.2011.11.001

Son DS, Hong JH, Chang SH, 2012. Determination of the autofrettage pressure and estimation of material failures of a Type III hydrogen pressure vessel by using finite element analysis. *International Journal of Hydrogen Energy*, 37(17):12771-12781. https://doi.org/10.1016/j.ijhydene.2012.06.044

Tan W, Falzon BG, Chiu LNS, et al., 2015. Predicting low velocity impact damage and compression-after-impact (CAI) behaviour of composite laminates. *Composites Part A: Applied Science and Manufacturing*, 71:212-226. https://doi.org/10.1016/j.compositesa.2015.01.025

Tsai SW, Wu EM, 1971. A general theory of strength for anisotropic materials. *Journal of Composite Materials*, 5(1):58-80. https://doi.org/10.1177/002199837100500106

Vasiliev VV, Krikanov AA, Razin AF, 2003. New generation of filament-wound composite pressure vessels for commercial applications. *Composite Structures*, 62(3-4):449-459. https://doi.org/10.1016/j.compstruct.2003.09.019

Wang L, Zheng CX, Luo HY, et al., 2015. Continuum damage modeling and progressive failure analysis of carbon fiber/epoxy composite pressure vessel. *Composite Structures*, 134:475-482. https://doi.org/10.1016/j.compstruct.2015.08.107

Xia M, Takayanagi H, Kemmochi K, 2001. Analysis of multi-layered filament-wound composite pipes under internal pressure. *Composite Structures*, 53(4):483-491. https://doi.org/10.1016/S0263-8223(01)00061-7

Xiao FQ, Wu YZ, Zheng JY, et al., 2017. A load-holding time prediction method based on creep strain relaxation for the cold-stretching process of S30408 cryogenic pressure vessels. *Journal of Zhejiang University-SCIENCE A (Applied Physics & Engineering)*, 18(3):871-881. https://doi.org/10.1631/jzus.A1600798

Xu P, Zheng JY, Chen HG, et al., 2010. Optimal design of high pressure hydrogen storage vessel using an adaptive genetic algorithm. *International Journal of Hydrogen Energy*, 35(7):2840-2846. https://doi.org/10.1016/j.ijhydene.2009.05.008

Zheng CX, Yang F, Zhu AS, 2009. Mechanical analysis and reasonable design for Ti-Al alloy liner wound with carbon fiber resin composite high pressure vessel. *Journal of Zhejiang University-SCIENCE A*, 10(3):384-391. https://doi.org/10.1631/jzus.A0820025

Zheng CX, Wang L, Li R, et al., 2013. Fatigue test of carbon epoxy composite high pressure hydrogen storage vessel under hydrogen environment. *Journal of Zhejiang University-SCIENCE A (Applied Physics & Engineering)*, 14(6):393-400. https://doi.org/10.1631/jzus.A1200297

Zheng JY, Liu PF, 2008. Elasto-plastic stress analysis and burst strength evaluation of Al-carbon fiber/epoxy composite cylindrical laminates. *Computational Materials Science*, 42(3):453-461. https://doi.org/10.1016/j.commatsci.2007.09.011

## Appendix A Transformation of stiffness matrix from on-axis coordinate (1, 2, 3) to the off-axis coordinate ($r$, $\theta$, $z$)

The transformation of the stiffness matrix $\boldsymbol{C}$ from an on-axis coordinate system to an off-axis

stiffness matrix $\bar{\boldsymbol{C}}$ can be obtained by using a stiffness transformation matrix written as (Xia et al., 2001; Zheng and Liu, 2008; Bakaiyan et al., 2009)

$$\bar{\boldsymbol{C}}=\left[T_{\sigma}(\alpha)\right]^{-1}\boldsymbol{C}T_{\varepsilon}(\alpha), \tag{A1}$$

$$T_{\sigma}(\alpha)=\begin{bmatrix} m^2 & n^2 & 0 & 0 & 0 & 2mn \\ n^2 & m^2 & 0 & 0 & 0 & -2mn \\ 0 & 0 & 1 & 0 & 0 & 0 \\ 0 & 0 & 0 & m & -n & 0 \\ 0 & 0 & 0 & n & m & 0 \\ -mn & mn & 0 & 0 & 0 & m^2-n^2 \end{bmatrix}, \tag{A2}$$

$$T_{\varepsilon}(\alpha)=\begin{bmatrix} m^2 & n^2 & 0 & 0 & 0 & mn \\ n^2 & m^2 & 0 & 0 & 0 & -mn \\ 0 & 0 & 1 & 0 & 0 & 0 \\ 0 & 0 & 0 & m & -n & 0 \\ 0 & 0 & 0 & n & m & 0 \\ -2mn & 2mn & 0 & 0 & 0 & m^2-n^2 \end{bmatrix}, \tag{A3}$$

where $m$=cos$\alpha$, $n$=sin$\alpha$, and $\alpha$ is the winding angle of the filaments from the vessel axis.

## 中文概要

**题　目：** 考虑自增强影响的 III 型复合材料气瓶连续损伤模拟及渐进失效分析

**目　的：** 成型后的金属内胆复合材料气瓶，即 III 型复合材料气瓶（以下简称气瓶），需采用自紧工艺来提高疲劳寿命。最佳自紧压力是自紧工艺的重要参数。本文旨在建立确定最佳自紧压力和气瓶渐进失效的有限元方法，研究自紧后气瓶纤维和基体损伤演化规律，并探讨自紧后气瓶复合材料层和金属内衬层的应力变化。

**创新点：** 1. 建立针对三维气瓶的 Hashin 失效准则和指数型损伤演化的渐进失效模型，并通过 ABAQUS-UMAT 隐式有限元方法确定气瓶最佳自紧压力；2. 通过渐进失效分析，揭示自紧后的气瓶纤维和基体损伤的损伤演化规律，并阐明自紧对气瓶渐进失效的影响。

**方　法：** 1. 基于连续损伤力学，建立三维 Hashin 失效准则和指数型损伤演化的渐进失效理论模型；2. 通过 ABAUQS-UMAT 二次开发用户子程序实现渐进失效理论模型，并开展气瓶渐进失效计算；3. 通过平板拉伸算例以及与气瓶试验数据对比，验证模型的准确性。

**结　论：** 1. 基体损伤首先出现在螺旋层，而纤维损伤首先出现在环向层。2. 除了自紧后的泄压阶段和自紧后重新加压至压力值等于自紧压力的升压阶段，有无自紧的气瓶损伤演化规律基本一致；而在上述泄压和升压阶段，基体损伤保持不变，说明经过自紧后的气瓶在工作压力下存在基体损伤。3. 当内压压力低于自紧压力时，自紧工艺才会影响气瓶应力分布；且随着压力的升高，基体损伤不变，内衬应力减少，纤维应力增加；此外，经过自紧的气瓶在工作压力下最大环向和轴向内衬应力减少且出现在筒体部分的两端。

**关键词：** 复合材料气瓶；损伤演化行为；Hashin 失效准则；有限元分析